arXiv:1911.01254v1 [physics.chem-ph] 4 Nov 2019

Site-selective and real-time observation of bimolecular electron transfer during photocatalytic water splitting

Alexander Britz,[*a,b,‡] Sergey I. Bokarev,[c] Tadesse A. Assefa,[a,◇] Éva G. Bajnóczi,[d] Zoltán Németh,[d] György Vankó,[d] Nils Rockstroh,[e] Henrik Junge,[e] Matthias Beller,[e] Gilles Doumy,[f] Anne Marie March,[f] Stephen H. Southworth,[f] Stefan Lochbrunner,[c] Oliver Kühn,[c] Christian Bressler,[a,b] and Wojciech Gawelda[*a,g]

Time-resolved X-ray absorption spectroscopy has been utilized to monitor the bimolecular electron transfer in a photocatalytic water splitting system for the first time. This has been possible by uniting the local probe and element specific character of X-ray transitions with insights from high-level ab initio calculations. The specific target has been a heteroleptic $[Ir^{III}(ppy)_2(bpy)]^+$ photosensitizer, in combination with triethylamine as a sacrificial reductant and $Fe_3(CO)_{12}$ as a water reduction catalyst. The relevant molecular transitions have been characterized via high-resolution Ir L-edge X-ray absorption spectroscopy on the picosecond time scale. The present findings enhance our understanding of functionally relevant bimolecular electron transfer reactions and thus will pave the road to rational optimization of photocatalytic performance.

1 Introduction

Efficient water splitting has gained increased scientific interest in the past years as a sustainable source of carbon-free fuels, which could become a future alternative to the existing fossil-based sources.[1] In particular, solar light-induced catalytic splitting of water into hydrogen and oxygen is a very promising approach yielding hydrogen fuel, which undergoes combustion without producing undesired CO_2.[2] However, the water splitting chemical reaction needs to overcome relatively high thermodynamical barriers associated with bond breaking and formation, as it requires the simultaneous evolution of oxygen and hydrogen. Among the various strategies that employ solar energy, promising approaches have been reported by using catalysts.[3] In particular, homogeneous catalysis is rapidly emerging in this field, and various protocols for the generation of oxygen[4] and hydrogen[5] from water have been published. A key challenge in this area is the design of more efficient photosensitizers (PS) that absorb visible light leading to charge-separated and long-lived excited states.[6] From the latter, the negative and the positive charge can be used for water reduction (hydrogen generation) and water oxidation (oxygen generation), respectively.

One key scientific issue is the development of new PS complexes, which can more efficiently harvest solar light and act efficiently as electron donor sources for the subsequent catalysis.[6] Iridium complexes such as the heteroleptic complex $[Ir^{III}(ppy)_2(bpy)]^+$, turned out to be promising candidates for PS in water splitting.[7,8] Gärtner et al. reported that this heteroleptic Ir PS results, in combination with iron carbonyl complexes as catalysts, in efficient homogenous systems for photocatalytic hydrogen generation.[9] They can show large turnover numbers and exceptionally high internal quantum yields exceeding 40%.[10,11] In order to replace the rare transition metals of the platinum group in the PS by more abundant and less expensive elements research shifts towards non-precious metals like copper and iron. A homogeneous photocatalytic system based on Cu(I) PS complexes has been reported recently.[12] It is one of few noble-metal-free photocatalytic systems so far, which have been successfully employed for proton reduction. Achievements towards catalytic applications have been also reported for a new class of Fe-based complexes with carbene ligands.[13] However, the performance of the non-precious sensitizers in homogenous water splitting is much worse than that of heteroleptic Ir PS. It is therefore crucial to understand the individual reaction steps in the Ir based systems and the possibly functional role of electronic and geometric structure changes for the reductive electron transfer in photocatalysis.

In this study we present the application of a suite of complementary time-resolved hard X-ray spectroscopies with picosecond (ps) temporal resolution, in combination with ab initio electronic structure calculations to study a fully functional photocatalytic system for solar hydrogen generation (Fig. 1). It includes triethylamine

[a] *European XFEL, Holzkoppel 4, 22869 Schenefeld, Germany. E-mail: wojciech.gawelda@xfel.eu*

[b] *The Hamburg Centre for Ultrafast Imaging, Luruper Chaussee 149, 22761 Hamburg, Germany*

[c] *Institut für Physik, Universität Rostock, Albert-Einstein-Str. 23-24, 18059 Rostock, Germany*

[d] *Wigner Research Centre for Physics, Hung. Acad. Sci., H-1525 Budapest, Hungary*

[e] *Leibniz-Institut für Katalyse an der Universität Rostock, Albert-Einstein-Str. 29a, 18059 Rostock, Germany*

[f] *Argonne National Laboratory, Argonne, Illinois 60439, USA*

[g] *Faculty of Physics, Adam Mickiewicz University, Umultowska 85, Poznań, 61-614, Poland*

[‡] *Present addresses: Stanford PULSE Institute, SLAC National Accelerator Laboratory, Menlo Park, CA 94025, USA and Linac Coherent Light Source, SLAC National Accelerator Laboratory, Menlo Park, CA 94025, USA. E-mail: abritz@slac.stanford.edu*

[◇] *Present address: Condensed Matter Physics and Materials Science Department, Brookhaven National Laboratory, Upton, NY 11793, USA*

† Electronic Supplementary Information (ESI) available: UV-vis absorption spectrum of IrPS, Lα X-ray emission spectroscopy, determination of excited state fraction, estimation of rate constants. See DOI: 10.1039/b000000x/

(TEA) acting as a sacrificial reductant (SR) that quenches the photoexcited $[Ir^{III}(ppy)_2(bpy)](PF_6)$ and a $Fe_3(CO)_{12}$ complex as the water reduction catalyst. Our study aims to complete the current picture [14,15] of the influence of geometric and/or electronic structures of long-lived (> 100 ps) charge-separated excited states on the system's performance. This includes the efficiency of light-harvesting, subsequent reductive quenching of the Ir-based PS by the SR molecules, and the intermolecular electron transfer to the water reduction catalyst (WRC). A deeper understanding of the structure-function relationship is critical for the development and optimization of PS complexes for efficient hydrogen production in molecular photocatalysis.

The function of this system and its constituents has been described previously in Refs [15–18], cf. Fig. 1. It involves a four-step process, in which the Ir-based PS absorbs a photon and is excited to an electronically excited state PS* (step I), which can be subsequently reduced by an electron transfer from TEA molecule yielding PS^- (step II). The next step involves another electron transfer to the WRC (step III), which then reduces a proton of a nearby H_3O^+ molecule to hydrogen (step IV).

The photocatalytic reaction steps reported here are initiated by excitation in the intense metal-to-ligand charge transfer (MLCT) bands in the near UV range around 350 nm. The complete UV-vis absorption spectrum of the IrPS complex is shown in Fig. S1 of the Electronic Supplementary Information (ESI). The photophysical and -chemical processes in the Ir-based PS complex, which take place upon the excitation into the singlet MLCT band at 355 nm are summarized in Fig. 2. The photoexcitation of the molecule occurs within the Franck-Condon regime from the singlet ground state S_0 to a singlet MLCT state labeled S_m. The lowest excited bright state corresponds to a $d_{x^2-y^2} \rightarrow \pi^*(\text{ppy})$ electronic transition. [19,20] Excitation is followed by an ultrafast relaxation via internal conversion (IC) and intersystem crossing (ISC) into the lowest triplet MLCT state of $d_{x^2-y^2} \rightarrow \pi^*(\text{bpy})$ character labeled T_1. Recently, ISC rates for similar Ir(III)-complexes were measured using femtosecond optical transient absorption spectroscopy [21] and time-resolved photoluminescence measurements. [21,22] It was found that the ISC and relaxation into T_1 state occurs within 70 - 100 fs. This triplet state has a long lifetime, which can be chemically tuned from some hundreds of nanoseconds to several microseconds. [9] Once in the long-lived T_1 state, the IrPS can be reduced to a doublet D_0 state by the SR and the excess electron residing on the $\pi^*(\text{bpy})$ orbital [20] can be transferred from the PS^- complex to the WRC, as shown in step III in Fig. 1. As a competing mechanism to the reduction, a radiative or non-radiative deactivation of the T_1 back into the ground state can occur. The photoluminescence lifetimes of the T_1 state in tetrahydrofuran (THF) solution both with and without the SR (present as a co-solvent in a THF/TEA mixture with a 5/1 volume ratio) were measured to be 370 ns and 13 ns, respectively. [14]

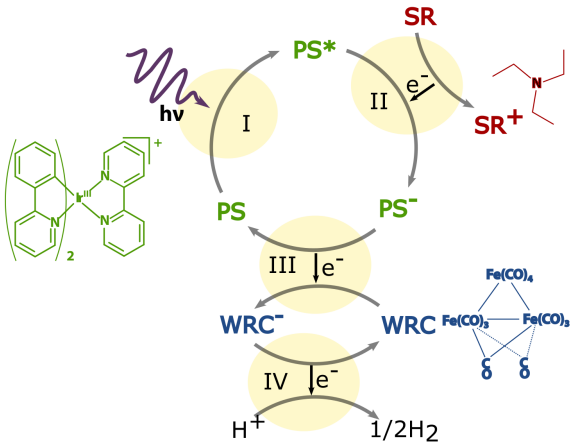

Fig. 1 Reaction cycle of a photocatalytic system consisting of a homogeneous solution of a sacrificial reductant (SR), a photosensitizer (PS) and a water reduction catalyst (WRC) for solar hydrogen generation [9,14–17]. The system discussed here consists of the PS $[Ir^{III}(ppy)_2(bpy)]^+$, triethylamine (TEA) as the SR and $Fe(CO)_{12}$ as the WRC.

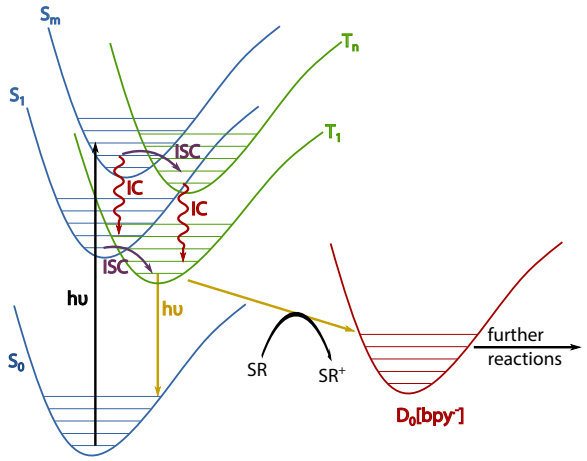

Fig. 2 Potential energy surface scheme of the relevant potentials as well as the photophysical and -chemical reactions of the $Ir[(ppy)_2(bpy)]^+$, adapted from Ref. 15. In the present study we focus on the dynamics of the reactive T_1 state and in particular the electron transfers involving the PS.

A complete study of the underlying photoinduced dynamics and more importantly the mechanistic aspects governing these processes at the PS and the WRC sites is often severely hindered when using only optical methods, since they are not sensitive to the oxidation state of the central metal ion and the molecular geometric structure. On the contrary, employing ultrafast X-ray spectroscopies allows accessing in an element-specific manner the active sites, i.e. the different metal ions, and to capture the transient electronic and geometric structure changes occurring during the photocatalytic function of the system. The present study is motivated by recent pump-probe X-ray absorption spectroscopy (XAS) investigations of oxidation states [23] and local geometric structures [23,24] of liquid-phase molecular systems. Also the spin state of the metal ion of such systems has been determined using time-resolved X-ray emission spectroscopy (XES). [25] Recently, picosecond- and femtosecond-resolved X-ray studies of a bimetallic donor-acceptor Ru-Co complex (a prototypical photocatalytic system) have shown how ultrashort hard X-ray spectroscopies can be efficiently used to follow both the intra- and intermolecular charge transfer processes at the optically silent sites of photocatalysts. [26,27]

2 Experimental Measurements

Time-resolved X-ray absorption spectra of $[Ir(ppy)_2(bpy)]^+$ were collected at the 7ID-D beamline of the Advanced Photon Source (APS) both in total fluorescence yield (TFY) as well as in the high-energy resolution fluorescence detection (HERFD)[28] mode. More details concerning the experimental setup and the pump-probe techniques available at this beamline can be found in Refs[24,29,30]. Here we will only briefly summarize the experimental conditions present during the pump-probe measurements, which allowed us to record high quality X-ray absorption and X-ray emission spectra of both the ground and excited states of the PS complex. The APS in 24 bunch mode delivered an average X-ray flux of 4×10^{11} photons/s at the Ir L_3-edge (11.2 keV) in pulses with a repetition rate of 6.5 MHz. The X-ray probe pulses were monochromatized to $\Delta E/E = 5\times\ 10^{-5}$ and focused to a spot of $4\times\ 5\ \mu m^2$ on the sample consisting of the sample solution in a 100 μm thick free flowing liquid jet. The optical pump laser repetition rate was set to 931 kHz, i.e. the 7th sub-harmonic of the X-rays. The inter-pulse spacing of 1.07 μs allows for a full ground state recovery between consecutive laser pulses. The laser wavelength was frequency tripled to 355 nm and laser pulses with 142 nJ energy were used to excite the sample. The laser focus was set to $13\times21\ \mu m^2$, thus slightly larger than the X-ray spot size, leading to a laser peak intensity of 6.6 GW/cm^2. TFY XAS were measured using a scintillation detector and simultaneously HERFD XAS were acquired to obtain XAS with sub core-hole lifetime limited energy resolution. The HERFD XAS were measured with a Johann[31] spectrometer employing a Ge(800) analyzer crystal to selectively detect photons at the Lα_1 peak energy of 9175 eV. Three different sample solutions were measured: i)15 mM of the pure PS in CH_3CN, ii)15 mM of the PS in a 1:4 mixture of TEA and CH_3CN and iii) 12.5 mM PS and 9 mM $Fe_3(CO)_{12}$ in a 1:5 mixture of TEA and CH_3CN. Here, CH_3CN is chosen as solvent since it provides a higher solubility for the PS than THF, which is used in the optimized catalytic system. It was previously shown that the photocatalytic system works also with CH_3CN as solvent, however, with lower yields.[10] The high PS concentration is necessary due to the thin sample thickness.

3 Theoretical Calculations

X-ray spectra originating from the ground singlet S_0 and first excited triplet T_1 electronic states were calculated in the dipole approximation at the first principles restricted active space self-consistent field (RASSCF) level and perturbative LS-coupling scheme for the spin-orbit coupling[32,33]. A relativistic ANO-RCC basis set[34,35] of triple-zeta quality for iridium and its first coordination shell and of double-zeta quality for other atoms was employed. For the detailed description of the protocol, see e.g. Ref. 36. The active space comprised three Ir 2p, two pairs of highly correlated σd bonding and σ^*d antibonding orbitals, three non-bonding d-orbitals, and one π^*(bpy) orbital (see Fig. 5b)), allowing description of the S_0 and T_1 states (originating from $d_{x^2-y^2} \rightarrow \pi^*(bpy)$ excitation) as well as Ir L-edge core excited states. This method should provide reliable results for transition metal compounds, where static electron correlation could play an important role[19] and due to its correlated nature is prerequisite to describe excited state (T_1) X-ray absorption. Spectra were calculated at equilibrium geometries of the S_0 and T_1 states taken from Ref. 19. Molecular orbital energies were calculated using long-range corrected density functional theory (LC-BLYP with a LANL2DZ/6-31G(d) basis set)[37] since RASSCF does not provide energies of canonical orbitals.

4 Results and Discussion

The TFY and HERFD XANES of the bare PS in CH_3CN (i.e. in absence of TEA and WRC) with and without laser excitation, the transient difference and the reconstructed excited state spectrum can be found in Fig. 3. The laser excited spectrum (Laser ON) has been determined to contain an excited state fraction of 12%, see ESI for details on the excited state fraction determination. This is used to reconstruct the excited state (ES) spectrum by removing the remaining (dominant) contribution of the ground state (GS) from the laser excited spectrum.

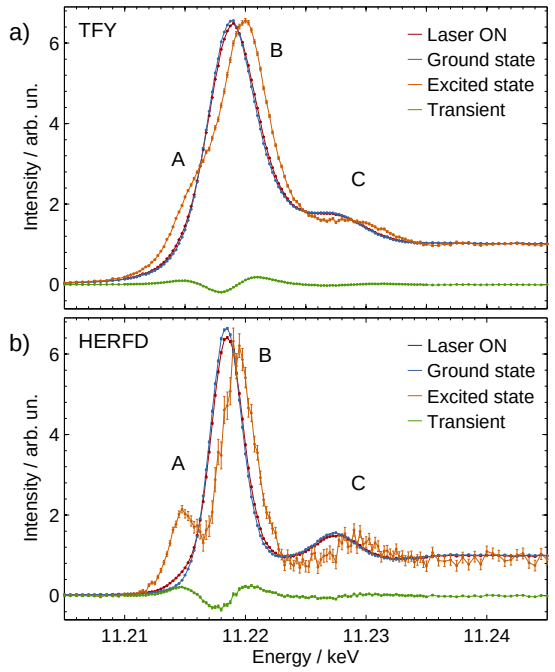

Fig. 3 L_3-edge XANES measured in a) TFY and b) HERFD of the laser excited ensemble (red), the ground state (blue), the reconstructed excited state (orange) and the transient difference (green) of $Ir[(ppy)_2(bpy)]^+$ in CH_3CN.

Table 1 Upper panel: Energies of L_3-edge XANES features, all energies are given in eV relative to the $2p_{3/2}$ ionization energy of 11215 eV. Lower panel: Energies of L_2-edge XANES features, all energies are given in eV relative to the $2p_{1/2}$ ionization energy of 12824 eV.

	A	B	C	edge
Ground state (L_3)		3.8±0.1	12.8±0.3	5.4±1.6
Excited state (L_3)	0.2±0.2	4.8±0.3	14.7±0.4	6.4± 8.8
Shift GS-ES (L_3)		+1.0±0.4	+1.9±0.5	+1.0± 9.0
Ground state (L_2)		2.7±0.1	11.7±0.1	4.5±1.1
Excited state (L_2)	-0.8±0.4	3.7±0.2	13.4±0.3	5.7± 3.3
Shift GS-ES (L_2)		+1.0±0.3	+1.7±0.4	+1.2± 3.5

The features of the TFY spectra are extremely broad due to

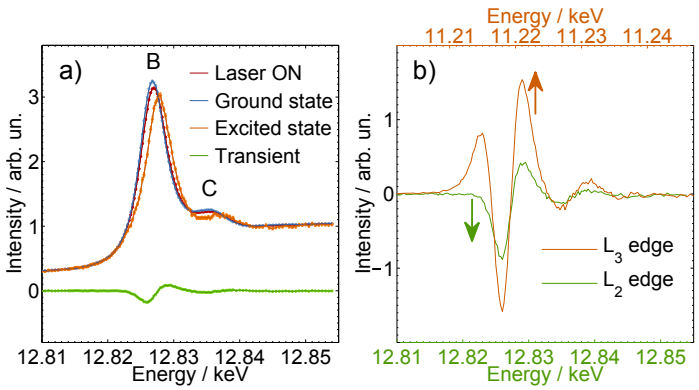

Fig. 4 a) TFY L_2-edge XANES of the laser excited ensemble (red), the reconstructed excited state (orange), the ground state (blue) and the transient difference (green) of $[Ir(ppy)_2(bpy)]^+$ in CH_3CN. In b), a comparison between this L_2-edge transient (green) to the L_3-edge transient (orange) is shown, the transients are normalized to the respective edge jump and scaled to 100 % excited state fraction.

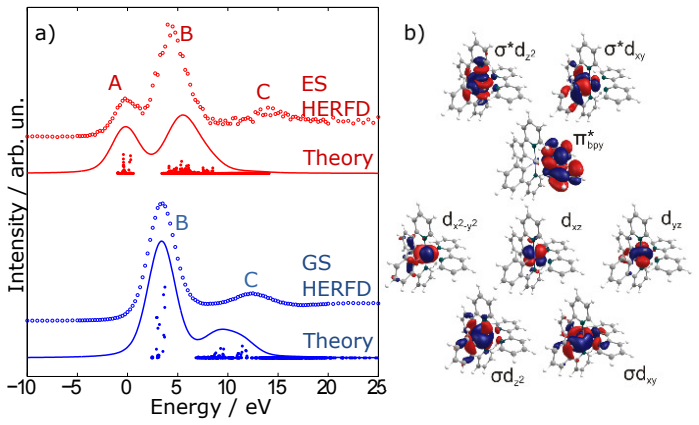

Fig. 5 Simulated L_3-edge XANES of the S_0 GS and the T_1 MLCT ES (a), the x-axis is given relative to the $2p_{3/2}$ ionization energy of 11215 eV. The orbital active space (apart from 2p orbitals) used for RASSCF calculations is shown in b).

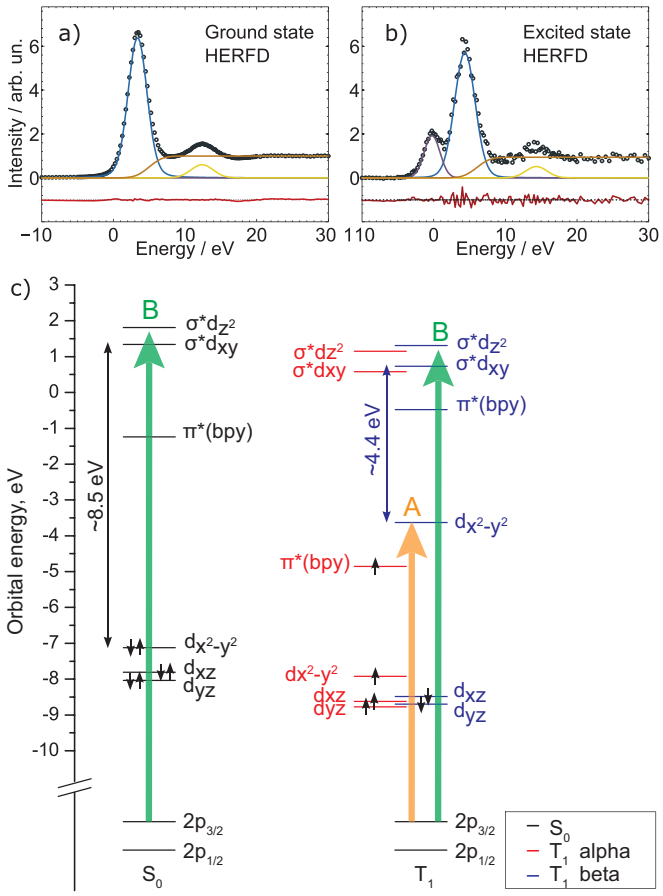

Fig. 6 Reconstructed HERFD XANES spectra together with measured data of $[Ir(ppy)_2(bpy)]^+$ in CH_3CN in its GS a) and ES b). The x-axis is given relative to the $2p_{3/2}$ ionization energy of 11215 eV. c) Diagram showing the relevant orbitals as computed with restricted (S_0) and unrestricted (T_1) density functional theory. The orbital manifold of the T_1 state contains two subsets: α orbitals occupied by spin-up electrons (red) and β ones with spin-down electrons (blue) which have different energies. The transitions of the L_3-edge for the GS involve the orbitals $2p_{3/2}$, $\sigma^* d_{z^2}$, and $\sigma^* d_{xy}$ (green arrow, band B) and for the ES additionally transition to spin-down $d_{x^2-y^2}$ (organge arrow, band A). The L_2-edge XANES contains the corresponding transitions starting from the $2p_{1/2}$ sub-shell (not shown with arrows).

the 5.25 eV L_3-edge core-hole lifetime broadening[38]. The HERFD spectra show an about 2 eV improved resolution of 3.0 eV - 3.5 eV and exhibit the same features as the TFY spectra. Thus for the further analysis we focus on the HERFD spectra in Fig. 3b). The prominent features of the spectra are labeled A, B and C, cf. Tab. 1. In the GS spectrum a very intense white line feature B around 11.219 keV and a second transition C at higher energy of about 11.229 keV are visible. The ES spectrum contains an additional peak A at a lower energy of about 11.215 keV, which is not visible in the GS spectra. Furthermore, B and C shift about 1 eV - 2 eV to higher energies in the ES compared to the GS, thus evidencing the oxidation of the Ir center from Ir^{III} to Ir^{IV}.

The L_2-edge measured in TFY is presented in Fig. 4a) and exhibits the same features in the GS as the L_3-edge. Nevertheless, in the ES a clear feature A is missing. The absence of this feature becomes even clearer when comparing the transient differences of the GS and the ES (see Fig.4b)), in the L_2-edge the first positive peak of the L_3-edge is not present.

The assignment of the L_3-edge features is made on the basis of RASSCF calculations. The comparison of the experimental and theoretical spectra for both ground and excited states can be found in Fig. 5a). The spectrum consists of several tens of transitions, with some of them having small intensity summing up to a notable feature due to their number. The assignment of multi-reference many-body RASSCF wave functions is quite involved due to their multiconfigurational character, which is additionally complicated by spin-orbit coupling. Here, for simplicity, the information is possibly reduced to transitions between single orbitals (Fig. 5b)), having however non-integer occupations. An orbital energy scheme for the relevant transitions discussed in the following is given in Fig. 6c).

The GS spectrum contains two features denoted as B and C in Fig. 5a) (blue line). Peak B mainly consists of $2p \rightarrow \sigma^* d_{z^2}$ and $2p \rightarrow \sigma^* d_{xy}$ transitions. Remarkably, some of the transitions having non-vanishing intensity are of $2p \rightarrow \pi^*(bpy)$ nature and

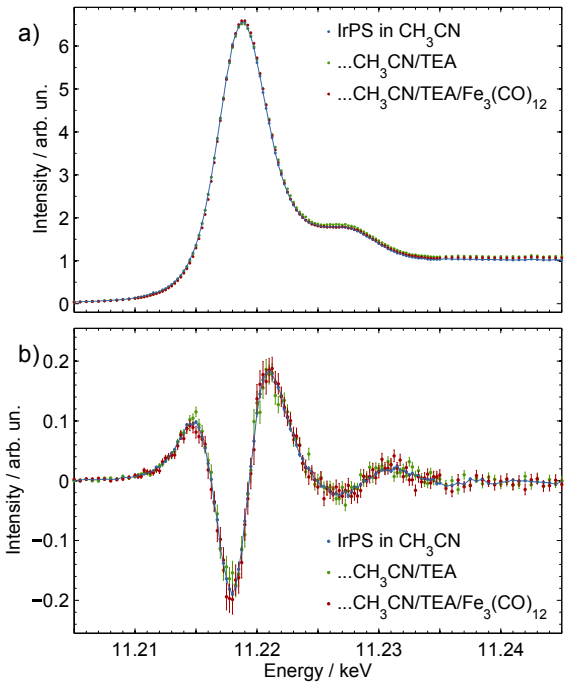

Fig. 7 Comparison of XANES of $Ir[(ppy)_2(bpy)]^+$ in CH_3CN (blue), as well as in CH_3CN/TEA (green) and in CH_3CN/TEA/$Fe_3(CO)_{12}$(red) mixtures, respectively. In a) the ground state spectra and in b) the transient differences 100 ps after excitation are shown. The static spectra and the transient differences are arbitrarily scaled in intensity to simplify comparison.

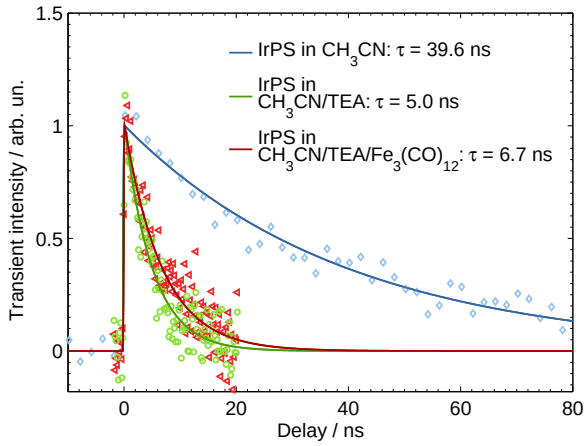

Fig. 8 Time delay scan of $Ir[(ppy)_2(bpy)]^+$ in CH_3CN (blue), as well as in CH_3CN/TEA (green) and CH_3CN/TEA/$Fe_3(CO)_{12}$ (red) mixtures. A fit of an exponential decay resulted in excited state lifetimes of (39.6±2.8) ns, (5.0±0.6) ns and (6.7±0.7) ns for the three samples, respectively.

can be considered as charge-transfer excitations. Peak C in turn is due to two-electron shake up transitions, where in the region of 7-10 eV $2p \rightarrow \sigma^* d_{z^2}$ transitions are occurring simultaneously with excitations from $d_{x^2-y^2}$ and d_{xz} orbitals to $\pi^*(bpy)$ ones. Transitions in 10-13 eV range are very similar but in this case $\sigma^* d_{xy}$ is accepting electron instead of $\sigma^* d_{z^2}$.

Features in the T_1 spectrum have similar nature to those of ground state spectrum with the only difference that triplet configuration has a hole in $d_{x^2-y^2}$ orbital and an additional electron in the $\pi^*(bpy)$ orbital. This fact gives rise to an additional feature A in excited state spectrum where transitions correspond mainly to $2p \rightarrow d_{x^2-y^2}$ excitation. This assignment is in agreement with that performed for the homoleptic $[Ru(bpy)_3]^{2+}$ complex with higher symmetry reported before.[23] The main type of transitions contributing to feature B is of $2p \rightarrow \sigma^* d_{z^2}$ and $2p \rightarrow \sigma^* d_{xy}$ nature. In addition to shake ups mentioned above, one sees also contributions from $d_{xz,yz} \rightarrow d_{x^2-y^2}$ and $\pi^*(bpy) \rightarrow \sigma^* d_{xy}$ because of additional hole/electron present in T_1 state. Interestingly, the low-energy flanks of bands A and B in T_1 spectrum have mainly spin-forbidden character gaining intensity due to spin-orbit coupling. This means that the initial state is mostly triplet, while the final ones are predominantly singlet.

To further quantify the exact energy positions of the XAS features, the HERFD XANES spectra have been fitted using a superposition of an arctan-broadened absorption edge and Voigt profiles for the discrete transitions. The corresponding transitions to the fit are shown in Fig. 6a) and b) and the obtained peak and edge position from this fit can be found in Tab. 1. The same fitting procedure has been applied to the L_2-edge TFY XAS (see ESI). The obtained energies corresponding to the features have been added to the table. The difference in the energies of the A and B transitions from the L_3-edge HERFD measurement results in a splitting between $d_{x^2-y^2}$ and both σ^* transition of (4.6±0.4) eV and is confirmed within the error bars by the respective features in the L_2-edge. The splitting is in good accord with the theoretical value reported in Figs. 5a) and 6c). Most importantly for the application of the time-resolved XAS measurements to the catalytic hydrogen production process, we are able to determine the 5d-orbital occupation allowing to directly monitor the optically induced charge separation with concomitant creation of a vacancy in the 5d-shell. This should in the next step allow for monitoring the arrival of an additional charge from the SR to the PS*.

The static TFY XANES spectra of the PS in CH_3CN, of the PS in the TEA/CH_3CN mixture and of the PS and with the $Fe_3(CO)_{12}$ in the TEA/CH_3CN mixture are indistinguishable within our experimental resolution, see Fig. 7. This allows us to conclude that the addition of the SR as well as of the WRC does not severely affect the geometric or electronic structure of the PS in the GS. The transient TFY XANES of all three samples are qualitatively similar as well, thus 100 ps after photoexcitation the PS is presumably in the same electronic state independent of the addition of the SR and the WRC.

Time delay scans of the excited state of these three samples have been taken at the energy of maximum transient intensity, i.e. at 11221.5 eV (see Fig. 8). A fit of a convolution of a Gaussian broadened step function with an exponential decay delivered MLCT excited state lifetimes of (39.6±2.8) ns, (5.0±0.6) ns and (6.7±0.7) ns for the PS in CH_3CN, the IrPS in the TEA/CH_3CN mixture and the PS together with the $Fe_3(CO)_{12}$ in the TEA/CH_3CN mixture, respectively. The ground state recovery time of (39.6±2.8) ns is shorter than the previously measured (60.2±0.4) ns.[39] This could be due to quenching of the excited state by oxygen, which in our

case is present due to the open jet setup, constantly exposing the sample solution to oxygen contained in the surrounding air. The lifetime shortening associated with the addition of TEA by a factor of 8 which is due to the electron transfer (ET) from TEA to the IrPS and a filling of the vacancy in the $d_{x^2-y^2}$-orbital. The slightly longer excited state lifetime of 7 ns in the fully functionally photocatalytic system can be attributed to the lower TEA concentration. Using the ES lifetime τ_0 without and τ with the TEA present we can calculate the TEA concentration c_{TEA} dependent quenching rate constant k_q of the ES via ET using the Stern-Volmer equation [14]

$$k_q(c_{\mathrm{TEA}}) = \frac{1}{\tau} - \frac{1}{\tau_0} = 1.76 \times 10^8 \ \mathrm{s}^{-1} . \quad (1)$$

With the TEA concentration $c_{\mathrm{TEA}} = 1.44$ M this results in a bimolecular quenching respectively electron transfer rate of $k_{\mathrm{ET}} = 1.22 \times 10^8$ $(\mathrm{Ms})^{-1}$. The ET rate for a diffusion limited reaction has been estimated to 2.06×10^{10} $(\mathrm{Ms})^{-1}$ (see ESI for details). According to this, only about every 170th encounter of a TEA molecule with an excited PS leads to an electron transfer process.

The results are well in line with previous findings obtained by time-resolved photoluminescence measurements on the PS. In that case quenching of the sensitizer phosphorescence by TEA was studied in tetrahydrofuran solutions. [14] A bimolecular quenching rate of 5.9×10^7 $(\mathrm{Ms})^{-1}$ was observed while the diffusion controlled collision rate was estimated to 1.4×10^{10} $(\mathrm{Ms})^{-1}$ indicating that only one out of 200 collisions results in a quenching event. This is in good agreement with the ET efficiency found in the present experiments. In the previous study also ab initio calculations on the collision complex were performed. [14] They indicate that only at specific collision geometries an ET is possible and only a small fraction of the collisions occurs with such a geometry. This can explain the small number of encounters resulting in ET. The advantage of the present measurements is that not only depopulation of a luminescent state is observed but the filling of the hole at the Ir atom by an electron from the SR proving the proposed ET step.

5 Conclusions

We have applied picosecond-resolved X-ray spectroscopies to investigate an Ir-based PS for photocatalytic hydrogen generation. Thereby functionally relevant bimolecular electron transfer steps in a homogeneous solution have been monitored for the first time. We were able to quantify the electronic structural changes of the PS as they take place during the photocatalytic cycle by mapping the (metal centered) unoccupied orbitals of the Ir PS in ground and excited states using mainly L_3-edge XANES. The features in the TFY spectra are extremely broadened due to the >5 eV core-hole lifetime and applying HERFD XANES enabled an improvement in the resolution of about 2 eV down to 3.0 eV - 3.5 eV. This allowed for an accurate analysis of XANES features and decomposing the edge into its main transitions, i.e. to accurately determine their energy positions and relative intensities. The detailed analysis was guided by high-level ab initio calculations of ground and excited state spectra. Equipped with this knowledge about relevant X-ray fingerprints, the Ir PS in the fully functioning photocatalytic system was investigated. Here, we were able to directly observe the bimolecular electron transfer process from TEA to the Ir PS via a reduction of the MLCT excited state lifetime of the Ir PS by a factor of about 8. More specifically, we can monitor the oxidation state of the Ir atom. After optical excitation and trapping in the MLCT state, the Ir^{III} ion is oxidized to Ir^{IV} leading to the appearance of a new band in the X-ray absorption spectrum. Upon bimolecular electron transfer from the sacrificial reductant the hole on the Ir 5D shell is refilled, yielding back Ir^{III} and its characteristic spectrum. Due to the element specifity the extra electron on the bpy ligand does not yield noticeable changes in the Ir L-edge spectrum. Hence, the present setup is not sensitive to the electron relay from the Ir PS to the WRC. Therefore, in future studies it would be desirable to also apply time-resolved X-ray absorption and emission at the Fe-edges of the WRC ($Fe_3(CO)_{12}$) to monitor also the last steps (III and IV) of the reaction cycle.

To summarize, the present proof-of-principle study has enhanced our understanding of functionally relevant bimolecular electron transfer reactions and thus will pave the road to rational optimization of the performance of homogeneous photocatalytic systems.

Conflicts of Interest

There are no conflicts to declare.

Acknowledgements

We thank Chris Milne and Jakub Szlachetko for their help with setting up the HERFD XAS measurements and for the loan of analyzer crystals, Frank de Groot and Pieter Glatzel for discussions regarding the interpretation of the HERFD XAS measurements as well as Daniel Haskel for the loan of the Ir(IV) reference.
This work is financed by the European XFEL, by the Deutsche Forschungsgemeinschaft (DFG) via SFB 925 (project A4), and by the Hamburg Centre for Ultrafast Imaging (CUI). AB acknowledges support from the International Max Planck Research School for Ultrafast Imaging and Structural Dynamics (IMPRS-UFAST), and we acknowledge the European Cluster of Advanced Laser Light Sources (EUCALL) within work packages PUCCA (CB), which has received funding from the European Union's Horizon 2020 research and innovation programme under grant agreement No 654220. WG acknowledges the National Science Centre (NCN) in Poland for grant SONATA BIS 6 No. 2016/22/E/ST4/00543. ZN, ÉGB and GV were supported by the 'Lendület' (Momentum) Program of the Hungarian Academy of Sciences (LP2013-59), the Government of Hungary and the European Regional Development Fund under grant VEKOP-2.3.2-16-2017-00015, and the National Research, Development and Innovation Fund (NKFIH) under contract FK124460. SIB and OK acknowledge financial support from DFG (grants BO 4915/1-1 and KU 952/10-1).

Author Contributions

WG, CB, OK, SL and AB designed the research; NR and NR synthesized the sample; NR, HJ and MB contributed to the conception; GD, AMM and SHS built the high-repetition rate pump-probe X-ray spectroscopy setup; AB, TA, EGB, ZN, GV, GD, AMM and SS performed the X-ray experiments; SIB performed the simulations; AB analyzed the experimental data; AB, SIB and WG wrote the manuscript wit contributions from all co-authors.

References

1 N. Armaroli and V. Balzani, *Angew. Chem., Int. Ed.*, 2007, **46**, 52–66.

2 N. S. Lewis and D. G. Nocera, *Proc. Natl. Acad. Sci. U. S. A.*, 2006, **103**, 15729–15735.

3 K. Sanderson, *Nature*, 2008, **452**, 400–402.

4 X. Sala, I. Romero, M. Rodríguez, L. Escriche and A. Llobet, *Angew. Chem., Int. Ed.*, 2009, **48**, 2842–2852.

5 M. Wang, Y. Na, M. Gorlov and L. Sun, *Dalton Trans.*, 2009, 6458–6467.

6 O. Bokareva, T. Möhle, A. Neubauer, S. Bokarev, S. Lochbrunner and O. Kühn, *Inorganics*, 2017, **5**, 23.

7 J. I. Goldsmith, W. R. Hudson, M. S. Lowry, T. H. Anderson and S. Bernhard, *J. Am. Chem. Soc.*, 2005, **127**, 7502–7510.

8 L. L. Tinker, N. D. McDaniel, P. N. Curtin, C. K. Smith, M. J. Ireland and S. Bernhard, *Chem. - Eur. J.*, 2007, **13**, 8726–8732.

9 F. Gärtner, S. Denurra, S. Losse, A. Neubauer, A. Boddien, A. Gopinathan, A. Spannenberg, H. Junge, S. Lochbrunner, M. Blug, S. Hoch, J. Busse, S. Gladiali and M. Beller, *Chem. - Eur. J.*, 2012, **18**, 3220–3225.

10 F. Gärtner, D. Cozzula, S. Losse, A. Boddien, G. Anilkumar, H. Junge, T. Schulz, N. Marquet, A. Spannenberg, S. Gladiali and M. Beller, *Chem. - Eur. J.*, 2011, **17**, 6998–7006.

11 H. Junge, N. Rockstroh, S. Fischer, A. Brückner, R. Ludwig, S. Lochbrunner, O. Kühn and M. Beller, *Inorganics*, 2017, **5**, 14.

12 S.-P. Luo, E. Mejía, A. Friedrich, A. Pazidis, H. Junge, E. Surkus, R. Jackstell, S. Denurra, S. Gladiali, S. Lochbrunner and M. Beller, *Angew. Chem., Int. Ed.*, 2013, **52**, 419–423.

13 T. C. B. Harlang, Y. Liu, O. Gordivska, L. A. Fredin, C. S. Ponseca, P. Huang, P. Chábera, K. S. Kjaer, H. Mateos, J. Uhlig, R. Lomoth, R. Wallenberg, S. Styring, P. Persson, V. Sundström and K. Wärnmark, *Nat. Chem.*, 2015, **7**, 883–889.

14 A. Neubauer, G. Grell, A. Friedrich, S. I. Bokarev, P. Schwarzbach, F. Gärtner, A.-E. Surkus, H. Junge, M. Beller, O. Kühn and S. Lochbrunner, *J. Phys. Chem. Lett.*, 2014, **5**, 1355–1360.

15 S. I. Bokarev, O. S. Bokareva and O. Kühn, *Coord. Chem. Rev.*, 2015, **304-305**, 133–145.

16 F. Gärtner, B. Sundararaju, A. E. Surkus, A. Boddien, B. Loges, H. Junge, P. H. Dixneuf and M. Beller, *Angew. Chem., Int. Ed.*, 2009, **48**, 9962–9965.

17 F. Gärtner, A. Boddien, E. Barsch, K. Fumino, S. Losse, H. Junge, D. Hollmann, A. Brückner, R. Ludwig and M. Beller, *Chem. - Eur. J.*, 2011, **17**, 6425–6436.

18 S. Fischer, O. S. Bokareva, E. Barsch, S. I. Bokarev, O. Kühn and R. Ludwig, *ChemCatChem*, 2016, **8**, 404–411.

19 S. I. Bokarev, O. S. Bokareva and O. Kühn, *J. Chem. Phys.*, 2012, **136**, 214305.

20 S. I. Bokarev, D. Hollmann, A. Pazidis, A. Neubauer, J. Radnik, O. Kühn, S. Lochbrunner, H. Junge, M. Beller and A. Brückner, *Physical Chemistry Chemical Physics*, 2014, **16**, 4789–4796.

21 G. J. Hedley, A. Ruseckas and I. D. W. Samuel, *J. Phys. Chem. A*, 2009, **113**, 2–4.

22 E. Pomarico, M. Silatani, F. Messina, O. Braem, A. Cannizzo, E. Barranoff, J. H. Klein, C. Lambert and M. Chergui, *J. Phys. Chem. C*, 2016, **120**, 16459–16469.

23 W. Gawelda, M. Johnson, F. M. F. D. Groot, R. Abela, C. Bressler and M. Chergui, *J. Am. Chem. Soc.*, 2006, 5001–5009.

24 G. Vankó, A. Bordage, M. Pápai, K. Haldrup, P. Glatzel, A. M. March, G. Doumy, A. Britz, A. Galler, T. A. Assefa, D. Cabaret, T. B. V. Driel, K. S. Kjær, A. O. Dohn, K. B. Moller, H. T. Lemke, M. Rovezzi, Z. Németh, E. Rozsályi, T. Rozgonyi, J. Uhlig, V. Sundstrom, M. M. Nielsen, L. Young, S. H. Southworth, C. Bressler and W. Gawelda, *J. Phys. Chem. C*, 2015, **119**, 5888–5902.

25 G. Vankó, P. Glatzel, V.-T. Pham, R. Abela, D. Grolimund, C. N. Borca, S. L. Johnson, C. J. Milne and C. Bressler, *Angew. Chem., Int. Ed.*, 2010, **49**, 5910–5912.

26 S. Canton, X. Zhang, J. Zhang, T. B. van Driel, K. S. Kjaer, K. Haldrup, P. Chabera, T. Harlang, K. Suarez-Alcantara, Y. Liu, J. Pérez, A. Bordage, M. Papai, G. Vankó, G. Jennings, C. A. Kurtz, M. Rovezzi, P. Glatzel, G. Smolentsev, J. Uhlig, A. O. Dohn, M. Christensen, A. Galler, W. Gawelda, C. Bressler, H. T. Lemke, K. B. Moller, M. M. Nielsen, R. Lomoth, K. Wärnmark and V. Sundström, *J. Phys. Chem. Lett.*, 2013, **4**, 1972–1976.

27 S. E. Canton, K. S. Kjaer, G. Vanko, T. B. van Driel, S.-i. Adachi, A. Bordage, C. Bressler, P. Chabera, M. Christensen, A. O. Dohn, A. Galler, W. Gawelda, D. Gosztola, K. Haldrup, T. Harlang, Y. Liu, K. B. Moller, Z. Nemeth, S. Nozawa, M. Papai, T. Sato, T. Sato, K. Suarez-Alcantara, T. Togashi, K. Tono, J. Uhlig, D. A. Vithanage, K. Warnmark, M. Yabashi, J. Zhang, V. Sundström and M. M. Nielsen, *Nat. Commun.*, 2015, **6**, 359.

28 K. Hämäläinen, D. Siddons, J. Hastings and L. Berman, *Phys. Rev. Lett.*, 1991, **67**, 2850–2853.

29 A. M. March, A. Stickrath, G. Doumy, E. P. Kanter, B. Krässig, S. H. Southworth, K. Attenkofer, C. A. Kurtz, L. X. Chen and L. Young, *Rev. Sci. Instrum.*, 2011, **82**, 73110.

30 K. Haldrup, G. Vankó, W. Gawelda, A. Galler, G. Doumy, A. M. March, E. P. Kanter, A. Bordage, A. Dohn, T. B. van Driel, K. S. Kjær, H. T. Lemke, S. E. Canton, J. Uhlig, V. Sundström, L. Young, S. H. Southworth, M. M. Nielsen and C. Bressler, *J. Phys. Chem. A*, 2012, **116**, 9878–9887.

31 H. H. Johann, *Zeitschrift für Physik*, 1931, **69**, 185–206.

32 P. A. Malmqvist, B. O. Roos and B. Schimmelpfennig, *Chem. Phys. Lett.*, 2002, **357**, 230–240.

33 S. I. Bokarev and O. Kühn, *WIREs Comput. Mol. Sci.*, 2019.

34 B. O. Roos, R. Lindh, V. Veryazov and P.-O. Widmark, *J. Phys. Chem. A*, 2004, **108**, 2851–2858.

35 B. O. Roos, R. Lindh, V. Veryazov and P.-O. Widmark, *J. Phys. Chem. A*, 2005, **109**, 6575–6579.

36 S. I. Bokarev, M. Khan, M. K. Abdel-Latif, J. Xiao, R. Hilal, S. G. Aziz, E. F. Aziz and O. Kühn, *J. Phys. Chem. C*, 2015, **119**, 19192–19200.

37 O. S. Bokareva, G. Grell, S. I. Bokarev and O. Kühn, *J. Chem. Theory Comput.*, 2015, **11**, 1700–1709.

38 M. O. Krause and J. H. Oliver, *J. Phys. Chem. Ref. Data*, 1979, **8**, 329–338.

39 S. Tschierlei, A. Neubauer, N. Rockstroh, M. Karnahl, P. Schwarzbach, H. Junge, M. Beller and S. Lochbrunner, *Phys. Chem. Chem. Phys.*, 2016, **18**, 10682–10687.